An improved modelling framework for strength and work hardening of precipitate strengthened Al–Mg–Si alloys

Feng Lu [a], Jonas K. Sunde [b], Calin D. Marioara [c], Randi Holmestad [b], Bjørn Holmedal [a,*]

[a] *Department of Materials Science and Engineering, Norwegian University of Science and Technology (NTNU), Alfred Getz Veg 2, NO-7491, Trondheim, Norway*
[b] *Department of Physics, Norwegian University of Science and Technology (NTNU), Høgskoleringen 5, NO-7491, Trondheim, Norway*
[c] *SINTEF Industry, NO-7465, Trondheim, Norway*

ARTICLE INFO

ABSTRACT

A modelling framework for the strength and work hardening contributions in age hardened Al–Mg–Si alloys is presented. The modelling work is based on transmission electron microscopy (TEM) measurements of the needle-shaped precipitate lengths and cross sections, and on stress-strain curves up to fracture, obtained by tensile tests applying a necking correction. For strains beyond the uniform limit, further work hardening is found to be strongly suppressed by the presence of the precipitates. At strains up to about 10–15%, new models are proposed for the description of the work hardening at different aging conditions. A detailed way of accounting for the contribution from generation of dislocation loops around non-sheared precipitates is formulated, based on the precipitate size and shape distribution. However, this mechanism overestimates the work hardening, and as an alternative, a new mechanism is suggested, assuming that the precipitates act as obstacles for moving dislocations and contribute to restrict their average slip length, leading to increased storage rate of the dislocations. The model captures measured stress-strain curves at different aging conditions well.

1. Introduction

The AA6xxx series Al–Mg–Si alloys gain their strength from precipitates, which nucleate, grow, and coarsen during thermal aging. Providing good ductility and corrosion resistance, these alloys play a key role in e.g., architectural and building products and are increasingly important as lightweight solutions in transport applications. Even though the material cost is higher than for steels, reduced manufacturing costs, favorable lifetime costs and lower carbon footprint make them competitive, e.g. for body-in-white applications [1]. Not only the initial yield strength is important but also the uniform elongation. An example is extruded profiles for building applications which are often delivered in T64 condition. It is less strong than the peak aged alloy but with a higher uniform elongation due to a stronger work hardening.

The strength of the age hardened alloys stems from the precipitates formed during aging. The alloy composition and the prior thermo-mechanical processing influence the shape, number density, size, and volume fraction of the precipitates. The metastable β'' phase is considered as the main strengthening phase in peak aged Al–Mg–Si alloys [2], though other precipitates may occur concurrently [3,4]. Several earlier works [5–10] have investigated the strengthening effect of these

precipitates. Rods or needle-shaped precipitates are formed with the length direction along <100> in the AlMgSi alloys [11]. Depending on the precipitate length, one precipitate needle may penetrate multiple {111} aluminum glide planes, and form dislocation obstacles at the intersections. A needle-shaped particle intercepts more glide planes than a spherical particle with the same volume and therefore contributes with more dislocation obstacles. Depending on needle cross section and type of precipitate, it contributes with either shearable or non-shearable obstacles for the moving dislocations. A critical size is commonly suggested as the shearable/non-shearable limit, often assumed to occur at a precipitate size close to the average size found at the peak aged condition [6,12,13]. Shearable precipitates can be cut by dislocations when their particle obstacle strength is exceeded. In an overaged state, most of the precipitates are strong and non-shearable, i.e., they have maximum obstacle strength.

In the strength model considered in the work by Deschamps et al. [14] and later by Myhr et al. [15,16], the mean obstacle strength was estimated from a model considering a volume distribution of spherical particles, where the needle shaped precipitates were converted to volume-equivalent spheres, defining the equivalent radius, which is the main parameter of this model. Esmaeili et al. [17] accounted for the

needle shape of the precipitates in the calculation of the yield strength, but then based on the average volume fraction and needle cross section, rather than on the detailed size distribution. Recently, both the aspect ratio and the length distribution of the needles are considered in the model by Holmedal [6], see also the recent discussion by Sunde et al. [18].

In strength models, a realistic estimation of the obstacle strength of shearable precipitates is challenging to obtain based on experiments and characterization. In practice it is handled by a simple model that is calibrated to estimate the correct stress levels for underaged conditions. The size and aspect ratios may be measured by TEM [18], or alternatively it can be estimated by modelling of diffusion controlled precipitation kinetics [5,19].

During deformation, the strength will increase. The dislocation/ precipitate-dislocation interactions raise the complexity of the work hardening of Al–Mg–Si alloys, due to the increased number of dislocation-based obstacles created during plastic deformation. The rate of increase is influenced by the presence of precipitates, which may alter the competition between dislocation storage and dislocation annihilations by dynamic recovery. The athermal storage is increased by storage of dislocation loops, either shear loops or prismatic loops, related to the bypassing of non-shearable precipitates, i.e. geometrically necessary dislocations (GNDs) [20]. In general, the storage rate of dislocations is inversely proportional to the mean free slip length, which decreases with the increased number of dislocation-based obstacles formed during plastic deformation.

It is reasonable to ask if a high number of precipitate-based obstacles affect the mean free slip length? This is an aspect not being paid attention to so far, but which is addressed in the model suggested here. However, in classical models, only the increased storage rate of GNDs generated around non-shearable particles are accounted for. This mechanism will increase the total storage rate of dislocations and correspondingly make the dislocation density increase faster. Unlike the precipitate-based obstacles, the dislocation-based obstacles are not thermally stable and can be annihilated during deformation, i.e., dynamic recovery. The dynamic recovery of the dislocations is, as a first approximation, based on the total dislocation density. Hence, due to the higher storage rate with GNDs, dynamic recovery will be invoked at smaller strains than without non-shearable precipitates. In a refined model, it has been suggested [21], that when prismatic loops are formed, the dislocation density near the non-shearable particles will increase locally and lead to earlier dynamic recovery in these regions. The influence on the dynamic recovery of the presence of a high number of shearable precipitates has not been considered so far, but when the density of particle-based obstacles become comparable to the density of dislocation-based obstacles, an interfering effect on the dynamic recovery might be expected.

Friis et al. [22] and more recently Ghosh et al. [23], applied the Nes model [24,25] for the evolution of the dislocation structures and corresponding work hardening of Al–Mg–Si alloys at various aging conditions. Friis et al. [22] predicted the precipitate distribution applying the model by Myhr et al. [15] for the strength contribution from the precipitates, while Ghosh et al. [23] applied a simpler estimate of this strength contribution, based on the volume fraction and average volume of the precipitates. More recent works by Myhr and co-workers [10,16, 26,27], combines various versions of the simplified Mechanical Threshold Strength (MTS) work-hardening model [28] with various versions of the same precipitation strength model. GNDs are accounted for, while the dynamic recovery of dislocations is assumed not to be affected by the precipitates. All these works add the stress contribution from precipitates to the term for dislocation strengthening linearly, i.e., the work hardening is treated independently of the strength contribution from the precipitates. However, since both dislocations and precipitates contribute with relatively strong obstacles, these stress terms should in theory be added quadratically, according to Kocks et al. [29]. Cheng et al. [30], analyzed the interactions between these two types of

hardening terms and suggested a nonlinear combination with an exponent between two (quadratic) and one (linear). For the evolution of the dislocation density estimates, they used a simplified version of the MTS model [28], while rough estimates were applied for the stress contributions from precipitates and elements in solid solution.

The work hardening is challenging to measure, since tensile tests of age hardened alloys neck at low strains. Still, this is important, since in forming or crash-performance simulations, stress-strain curves are required as model input for strains significantly beyond the onset of necking. Some works simply extrapolate the Voce equation [31] for the stress until fracture or fit the flow stress until fracture by inverse modelling [32] or combine other advanced methods [33,34]. A direct experimental method can be to use a low-friction compression test [35], which however is limited by the barreling instability induced by the friction. Another method, that will be applied here, is to apply necking corrections for uniaxial tensile tests, based on optical measurements of the necking contour [36–38].

The aim of the present study is to analyze a modelling framework for predicting strength and work hardening of an Al–Mg–Si alloy. The experimental work to be considered here, was reported earlier by Sunde et al. [18], and the part of it required here is presented in Chapter 2. It consists of extensive measurements of precipitate size and cross section distributions by TEM and tensile testing with stress-strain curves up to fracture obtained by necking corrections. In Chapter 3, the modelling framework is formulated. The precipitate strength term is based on a model recently suggested by Holmedal [6]. This model considers the needle shape of the precipitates in terms of length and thickness distributions quantified by TEM measurements. During deformation, the number of dislocation-based obstacles increases, while the number of obstacles due to the precipitates remains constant. The model predictions of initial strength and work hardening depend on how the mixture of these two types of obstacles are handled. A more refined version of the modelling approach by Cheng et al. [30] is developed, where the GNDs due to Orowan looping of the non-shearable precipitates are precisely accounted for by applying the measured size distribution of the precipitates. Furthermore, another mechanism for slip-length restrictions by the precipitates is suggested and tested. The results are presented and discussed in Chapter 4. Based on that, conclusions are made in Chapter 5.

2. Experiments

The Al–Mg–Si alloy, AA6082, was received from Neuman Aluminium Raufoss as extruded cylinders with cross-sectional diameter of 30 mm. The chemical composition is provided in Table 1.

A thorough TEM investigation and tensile tests of the same alloy and the same aging treatments as considered here, were reported earlier by Sunde et al. [18]. Hence, only a summary of these results is given. All specimens were solution heat treated in a salt bath at 540 °C for 12 min, followed by water quenching. After 10 min at room temperature, the specimens were artificially aged in an oil bath at 180 °C to various aging times, listed in Table 2. The alloy reached peak strength after 3 h aging. X-ray diffraction analyses showed no sign of recrystallization after the heat treatments. The grain size was determined to be approximately 23 μm, by line intercept in the radial direction, from light optical microscopy. Manganese-containing dispersoids were formed prior to extrusion, during the homogenization treatment, i.e. 2 h heating to 560 °C and subsequently 2 h holding time at this temperature before air cooling. The dispersoids remain thermally stable during the aging treatment of the alloy. Their mean radius was approximately $r_{disp} \approx 46 \pm 1$ nm and

Table 1
Nominal chemical composition (wt. %/at. %) of the AA6082 alloy.

Alloy	Si	Mg	Cu	Fe	Mn
Al–Mg–Si	0.88/0.85	0.72/0.80	0.03/0.01	0.24/0.12	0.51/0.25

Table 2
The aging times selected for TEM studies.

20 min	3 h	12 h	24 h	1 week	2 weeks	1 month

their volume fraction was approximately $f_{disp} \approx 0.85\% \pm 0.09\%$, based on TEM measurements of about 550 particles.

2.1. Precipitate length distributions

Details about the TEM work are referred to Sunde et al. [18]. Precipitate parameters, such as lengths and cross-sectional areas, were measured from bright-field TEM images acquired in the <100> Al zone axis. Fig. 1 shows an example of two TEM images of the precipitate microstructure at the peak aged condition and a schematic drawing of a typical electron energy loss spectroscopy (EELS) spectrum, including the formula used in Sunde et al. [18] to calculate sample thickness for each TEM image. For each ageing condition, roughly 200 to 400 precipitate lengths were measured, as well as 70 to 150 cross-sectional areas.

For representing the size distribution of the N_A measured precipitates, for simplicity, the two parameters of a log-normal distribution can be calibrated [7,22,39], or a Gaussian distribution may be applied [40]. More precisely, one can divide the sizes into classes of a certain bin-size and plot histograms. In our previous work [18] on this alloy, histograms were shown and log-normal distributions calibrated. However, in the current work, a kernel density estimator (KDE) is applied with a Gaussian kernel. Firstly, an uncorrected KDE, $\widehat{\varphi}_l$, is written as:

$$\widehat{\varphi}_l = \frac{1}{N_A} \sum_{i=1}^{N_A} \frac{\sqrt{2} \exp\left(-\frac{1}{2}\left(\frac{l-l_i}{h}\right)^2\right)}{\left(1 + \text{erf}\left(\frac{l_i}{\sqrt{2}h}\right)\right) h\sqrt{\pi}} \tag{1}$$

Note that $\int_0^\infty \widehat{\varphi}_l dl = 1$. Here h is the kernel bandwidth, estimated by Scott's Rule [41]:

$$h \approx d \cdot N_A^{-0.2} \cdot \sigma_l \tag{2}$$

The standard deviations σ_l of the precipitate length (l) distribution is obtained from the TEM data, and $d = 0.8$ is a constant. A correction of the KDE is suggested, to ensure that φ_l goes towards zero at $l = 0$. A normal distribution $\widehat{\varphi}_l(0)\exp(-0.5(l/h)^2)$, i.e., a kernel centred on $l = 0$ with width h, is subtracted from $\widehat{\varphi}_l$. This is safe in terms of keeping the distribution positive valued for $l > 0$. However, the new distribution must be renormalized to ensure that $\int_0^\infty \varphi_l dl = 1$.

$$\varphi_l = \frac{\widehat{\varphi}_l - \widehat{\varphi}(0)\exp\left(-\frac{1}{2}\left(\frac{l}{h}\right)^2\right)}{1 - \frac{1}{2}h\sqrt{2\pi}\widehat{\varphi}(0)}, l \geq 0 \tag{3}$$

Fig. 2 presents the precipitate needle-length distributions at various aging conditions. Both histograms, KDE estimates and a fitted log-normal distribution are compared in the figure, showing particle distributions counted from TEM measurements from alloy specimens aged
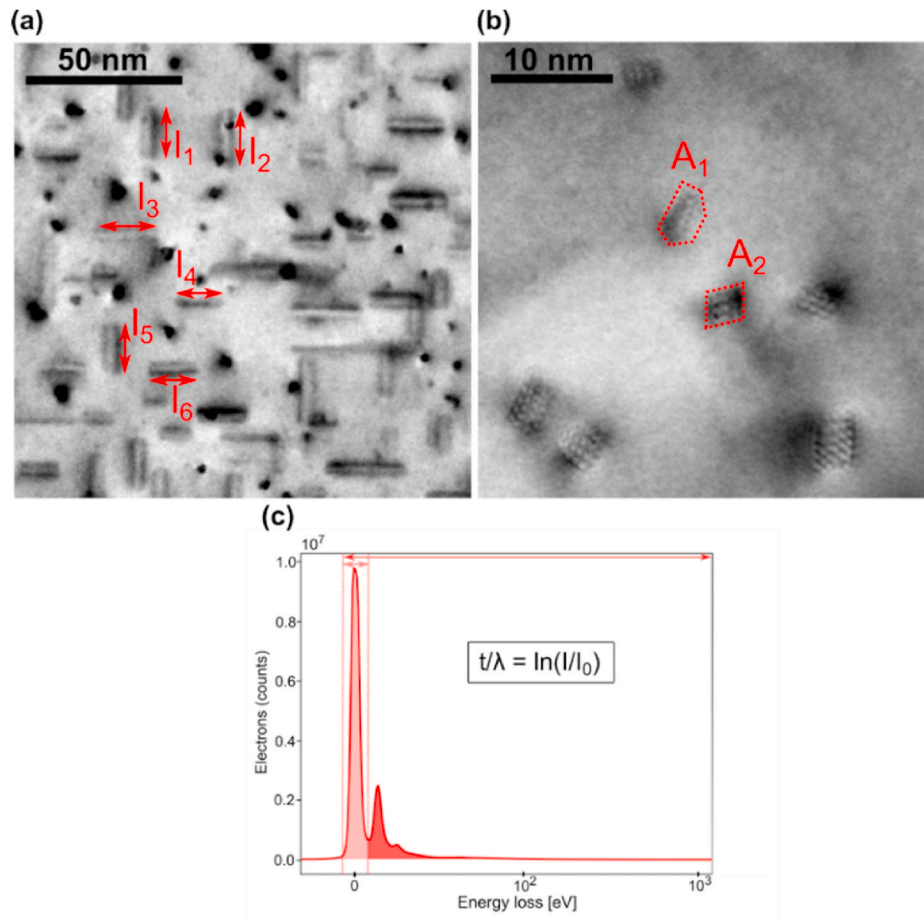

Fig. 1. Bright-field TEM images acquired in the <001> Al zone axis at the 3 h aging condition. Measurements of precipitate lengths (a) and cross-section areas (b) are indicated. In (c) a schematic drawing of a typical electron energy loss spectroscopy (EELS) spectrum is shown, with the formula used to calculate sample thickness for each TEM image.
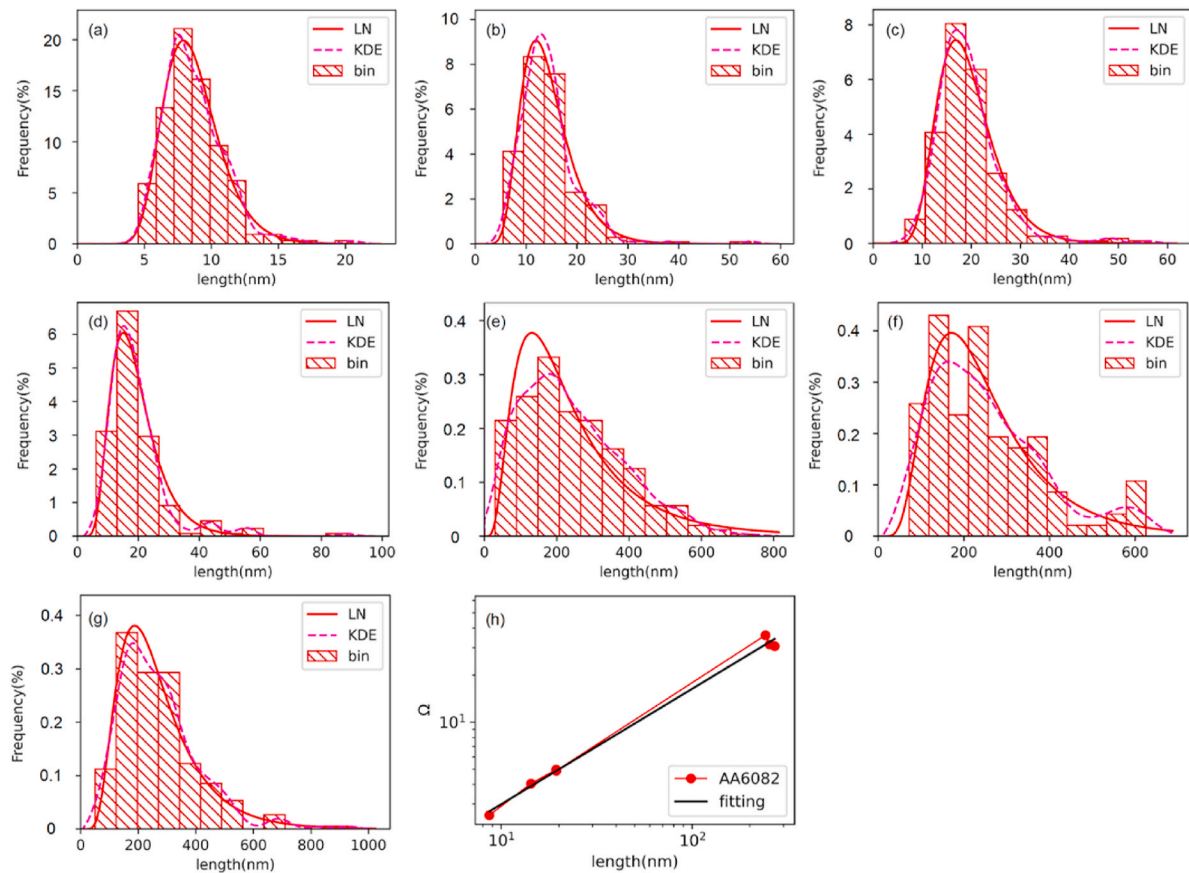
Fig. 2. Histograms, KDE (purple dashed line) and a best fit of a log-normal distribution (red line) for the precipitate length distributions. The statistics are from TEM measurements of a specimen aged at 180 °C for (a) 20 min, (b) 3 h, (c) 12 h, (d) 24 h, (e) 1 week, (f) 2 weeks, (g) 1 month. (h) shows the aspect ratio $\Omega = \bar{l}/\sqrt{\bar{a}}$ based on the mean length and cross section area at the different aging times. (For interpretation of the references to colour in this figure legend, the reader is referred to the Web version of this article.)

at 180 °C. The log-normal distribution provides a very good fit at the underaged and peak aged conditions, while at overaged conditions one or two smaller additional peaks appear at larger precipitate lengths. The detailed TEM observations in Fig. 3, indicate the presence of several precipitate phases, present already in the peak aged condition. As the β''

particles become relatively fewer at overaged conditions, they do not dominate the size distribution that much anymore. The log-normal distribution can only fit the main peak, which is due to the β'' particles. Both the KDE and the histogram rely on a well-chosen bin size or kernel width. The KDE applying Scott's Rule to estimate the kernel
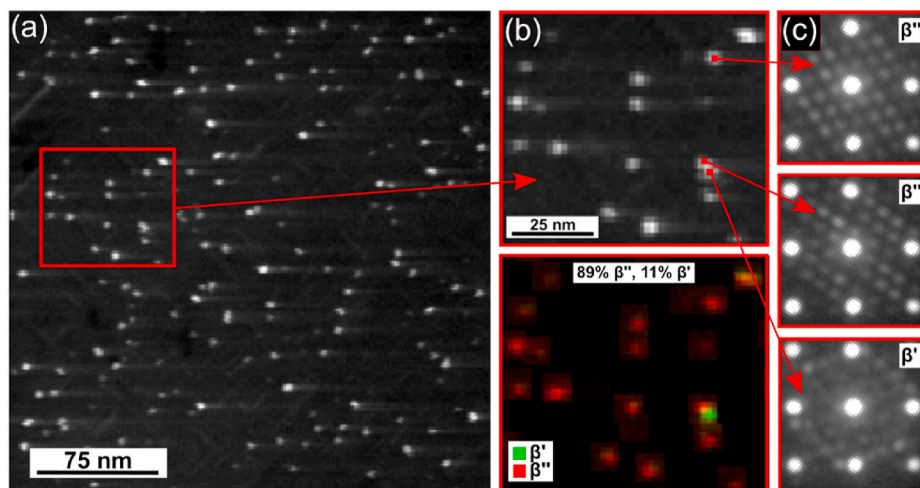

Fig. 3. (a) Example of virtual dark-field image formed from a SPED scan acquired in the [001] Al zone axis at the 3-h aging condition. (b) Selected region from SPED scan with phase mapping results shown below. (c) PED raw data patterns from indicated pixels in (b) showing characteristic diffraction patterns from β'' and β' precipitate phases, see Ref. [42] for details about this technique.

bandwidth, is expected to give the most precise description of the distributions. Note that the distributions here are normalized, hence the number density of precipitates N_v is required as an additional information for each aging condition. These are given in Table 3.

In the model, it is assumed that the aspect ratio of the precipitates, Ω, depends on the length of the precipitates. Hence, Ω can be estimated based on measurements of the average cross-section area and average particle length at various aging times, as shown in Fig. 2(h). The coefficients c and m are estimated based on a least squares fit of Equation (7) to this curve, giving $c = 0.55$ and $m = 0.74$.

2.2. Approximation of solute levels in the precipitates and in the Al matrix

The crystal structures and the chemical compositions of the Al–Mg–Si(-Cu) precipitate phases are known to a large extent [28–30]. Based on scanning precession electron diffraction (SPED), the fractions of the solutes contained in precipitate phases were estimated in Ref. [18]. Fig. 3 shows an example of the result of a SPED scan of a peak aged sample. For the region selected, it is seen that the precipitates are mainly of β'' type (red), as expected, but that there are also some few β' precipitates present (green).

Having firstly estimated the solute levels contained in the precipitates for a given aged condition, also the levels of atoms in solid solution in the matrix were estimated in Ref. [18], from the alloy's chemical composition, as the counterpart of the amount in precipitates and dispersoids. The Si atoms being part of primary particles formed during casting and the dispersoids formed during the homogenization of the alloy, remain stable during further aging heat treatments. This amount depends on the homogenization procedure and was estimated using the Alstruc model [43,44]. Alternatively, a simpler rule of thumb [22] could have been used for a rougher estimate of the Si content.

Table 4 summarizes the solute fraction of each element reported in Ref. [18], both as part of precipitates and as atoms in solid solution. The fraction of Si consumed by primary particles and dispersoids during casting and homogenization, as estimated by the Alstruc-model, was accounted for and the estimated Si-concentration in the matrix after casting and homogenization was 0.72/0.7 wt%/at%. With increased aging time, Si, Mg, and Cu are consumed by the precipitates, while the concentration of elements in solute solution is decreasing.

2.3. Tensile testing

Uniaxial tensile tests were performed at room temperature, and the results are reported in Ref. [18]. An open-source software [45] was applied for continuously measuring the geometry change of the specimen during the test, i.e. the radius of the minimum cross-sectional area and the radius of curvature of the necking contour. A detailed description of the software and its algorithms are given in Ref. [38]. A two-parameter equation [46] was applied to fit the ratio between these two radii as a function of the tensile strain and applied for a necking correction, according to Ref. [47], for determining true stress-strain curves beyond necking and until fracture. The resulting stress-strain curves were fitted by a four-term Voce equation, for which the parameters are tabulated in Ref. [18].

Fig. 4 (a) shows stress-strain curves, subtracted the initial yield stress to emphasize the work hardening, up to the onset of necking. The 3 h peak aging and the 12- and 24-h aging conditions give curves with less work hardening compared both to the more overaged conditions and to the underaged condition after 20 min aging. Fig. 4(b) presents the stress-strain curves all the way until fracture, obtained by using the necking corrections for each aging condition.

Stress-strain curves up to large strains at room temperature are commonly analyzed in terms of stage II, III and IV work hardening and saturation at sufficiently large strains, [48]. The stages are more easily recognized in the Kocks-Mecking (KM) plot in Fig. 4(c) than in the corresponding stress-strain curves in Fig. 4(b). An ideal stage II corresponds to linear initial work hardening, which is seldom seen at room temperature, but which occurs at very low temperatures for tensile tests of single crystals. However, the initial plateau in the KM plot in Fig. 4(c) for the 3-,12- and 24-h conditions, and the corresponding, almost linear stress-strain curves plotted up to the uniform strain limit in Fig. 4(a), can be interpreted as stage II behavior. Stage III corresponds to a linear decay in the KM plot and is clearly recognized for all cases in Fig. 4(c). In pure metals or in alloys with elements in solid solution tested at room temperature, stage III typically lasts for strains up to 50–100%, at which the work hardening saturates towards a constant stress-strain slope, typically 30–40 MPa for aluminum alloys [49]. This is the characteristic plateau in the KM-plot for linear stage IV behavior. However, as seen from Fig. 4(b), stage III ends at considerable smaller strains for the aged and ssss conditions, shortly after reaching the uniform strain, at less than 20% strain for all cases. The peak age condition (3 h) has a strong stage III work hardening but no stage IV. Instead, the curve reaches stress saturation right after the end of stage III. For the other conditions, a clear stage IV is seen, with a work hardening rate comparable to stage IV in other aluminum alloys but occurring at a much smaller strain than in non-heat treatable alloys.

3. Mechanical modelling

The stress contributions from the different mechanisms are often simply added together [15,50]. Consider the combination of two sets of dislocation obstacles, say of densities ρ_1 and ρ_2 with corresponding individual stress contributions $\sigma_1 = \alpha_1 \mu b \sqrt{\rho_1}$ and $\sigma_2 = \alpha_2 \mu b \sqrt{\rho_2}$. Then, if their obstacle strength and obstacle density are about the same, it would be inconsistent to add them, i.e., $\alpha_1 \mu b \sqrt{\rho_1} + \alpha_1 \mu b \sqrt{\rho_2} \neq \alpha_1 \mu b \sqrt{\rho_1 + \rho_2}$. In this case $\sigma^2 = \sigma_1^2 + \sigma_2^2$. However, in cases of one set of weak obstacles, e.g., solutes, and one set of strong obstacles, an additive rule is justified. The dislocation-based obstacles are rather strong and of comparable density as non-shearable precipitates, hence the quadratic rule applies at overaged conditions. At early-stage precipitation, the clusters and early-stage precipitates are more similar to solutes, and their stress contributions should be added linearly. Underaged conditions can be anywhere between these two extremes, and a pragmatic approach, similar as the one used by Cheng et al. [30], will be applied:

$$\sigma_f = \sigma_0 + \sigma_{ss} + \left(\sigma_p^n + \sigma_d^n \right)^{\frac{1}{n}} \tag{4}$$

The exponent n is a parameter between 1 (corresponding to weak obstacles) and 2 (corresponding to strong obstacles from the precipitates). Here σ_{ss}, σ_p and σ_d are the flow-stress contributions from solid solution, precipitation, and dislocations, respectively. Furthermore, σ_0 is a stress contribution to account for other stress contributions. The Peierls stress is negligible in fcc, hence the initial yield stress can be as low as a few MPa in coarse grained high-purity aluminum alloys. The Hall-Petch constant is small for aluminum [51], about 0.07 MPa$\sqrt{m}$, for the extruded alloys like those considered here with grain size of about 5–10 μm, this contribution is about 10–20 MPa. As shown by Zhao et al. [52], small amounts of Fe and Si increases the strength significantly,

Table 3
The number density of precipitates in each aged condition, from Ref. [18].

Aging time	20 min	3 h	12 h	24 h	1 week	2 weeks	1 month
N_v (μm^{-3})	73,240	67,024	49,247	46,489	1498	1130	1021

Table 4

The amount of Si, Mg and Cu (wt.%/at.%) as part of the precipitates (p) and in solute solution (ss). The condition ssss (super-saturated solid solution) indicates the as-quenched condition, from Ref. [18].

| Element	Aging time							
	ssss	20 min	3 h	12 h	24 h	1 week	2 weeks	1 month
Si (p)	0/0	0.29/0.287	0.4/0.392	0.42/0.400	0.42/0.412	0.4/0.389	0.46/0.445	0.48/0.469
Mg (p)	0/0	0.26/0.287	0.36/0.399	0.33/0.410	0.39/0.429	0.45/0.506	0.5/0.557	0.52/0.583
Cu (p)	0/0	0.003/0.001	0.0078 0.0026	0.009/0.003	0.012/0.004	0.015/0.005	0.021/0.007	0.027/0.009
Si (ss)	0.72/0.7	0.4/0.383	0.29/0.278	0.27/0.27	0.26/0.258	0.29/0.281	0.23/0.225	0.21/0.201
Mg (ss)	0.72/0.80	0.46/0.513	0.36/0.401	0.39/0.39	0.33/0.371	0.27/0.294	0.22/0.243	0.2/0.217
Cu (ss)	0.03/0.01	0.027/0.009	0.0222/0.0074	0.021/0.007	0.018/0.006	0.015/0.005	0.009/0.003	0.003/0.001
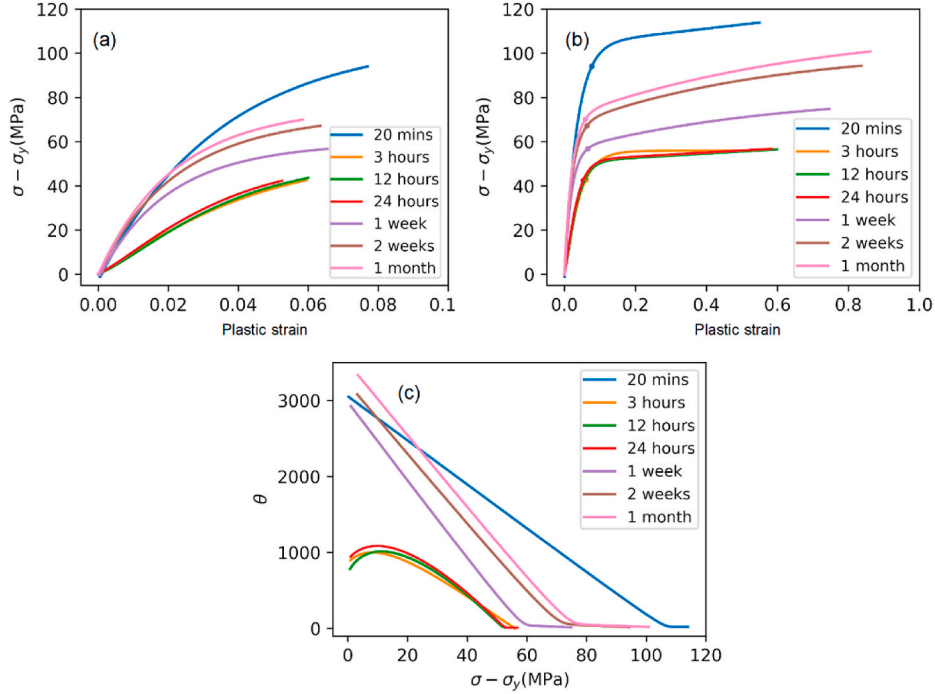
Fig. 4. Comparison of stress-strain curves (a) up to the onset of necking and (b) until fracture. In (c), the work hardening rate is shown as a function of the flow stress, i.e., a Kocks-Mecking plot.

approximately 10 MPa, which here is also accounted for by the term σ_0.

3.1. Needle-shaped precipitate strengthening

The stress estimate by Holmedal [6] is based on the dislocation simulations by Vaucorbeil et al. [53,54], from which the following stress expression was obtained:

$$\sigma_p = M\tau = \alpha_p M\mu b \sqrt{n_p} \bar{f}^{\frac{3}{2}}\left(1 - \frac{1}{6}\bar{f}^5\right) \qquad (5)$$

Here $M = 3.05$ is the Taylor factor, calculated from the measured extrusion texture, using the ALAMEL crystal-plasticity model [55]. Furthermore, $\mu = 27$GPa is the shear modulus and $b = 0.286$ nm the Burgers vector of the alloy. Note that the shear modulus applied in Ref. [6] by a mistake was put unrealistically low, hence a higher one is applied here, similar as in Refs. [15,50]. The constant α_p equals 0.9 according to simplified discrete dislocation simulations by Vaucorbeil et al. [53,54]. However, the due to simplified estimates for e.g. the dislocation line tension, slightly other values might be justified. A needle-shaped precipitate of length l penetrates several parallel {111} slip planes and contributes with an increasing number of dislocation-based obstacles. For this case, in the strength estimate by Equation (5), $n_p = \sqrt{3}N_v\bar{l}/3 = f_v/(\sqrt{3}\bar{a})$ is the number density of

precipitate-based obstacles per area slip plane, where f_v is the volume fraction of the precipitates, $\bar{a}$ is the average cross-sectional area of the precipitate needle, and $\bar{f}$ is the mean non-dimensional obstacle strength, where $0 \leq \bar{f} \leq 1$, [56].

The obstacle strength of each precipitate-based obstacle depends on the cross-sectional area that the dislocation must cut through. Precipitates with a cross-sectional area larger than a critical value a_c, are non-shearable, for which $f = 1$. The following model is used for estimating the cutting strength:

$$f = \min\left(\left(\frac{a}{a_c}\right)^\kappa, 1\right) \qquad (6)$$

Here $\kappa = 2$, is an empirical parameter, and the average cross-sectional area of precipitate needles at the peak-aged condition is assumed as the critical size for the point, from which the precipitates can be regarded as obstacles of maximum strength. It is reasonable to assume that this corresponds to the shearable/non-shearable transition. However, the strength can be at this high level also for shearable precipitates that are difficult to shear. Hence a_c does not necessarily directly correspond to the shearable/non-shearable transition. In this work $a_c = 12.5$nm^2 is used. The model [6] assumes a correlation between the length and cross section of the needle-shaped precipitates. An empirical relation is assumed for the aspect ratio Ω is as a function of the average

precipitate length $\bar{l}$:

$$\Omega = \frac{l}{\sqrt{a}} = \max(c\bar{l}^m, 1) \tag{7}$$

Here c and m are two coefficients that must be calibrated. The bookkeeping and estimates required for Equation (3) were worked out in Ref. [6], where the mean obstacle strength of the precipitates is estimated from the statistical distribution of the measured precipitate lengths, φ_l. Note that here the distribution $\int_0^\infty \varphi_l dl = N_v$ is not normalized, hence $\varphi_l \approx N_v \varphi_l$

$$\overline{f} = \frac{\int fA dn_p}{\int A dn_p} = \frac{\int_0^\infty fl\varphi_l dl}{\int_0^\infty l\varphi_l dl} = \left(\frac{1}{a_c^\kappa} \int_0^{\Omega_c\sqrt{a_c}} \frac{l^{2\kappa+1}}{\Omega(l)^{2\kappa}}\varphi_l dl + \int_{\Omega_c\sqrt{a_c}}^\infty l\varphi_l dl \right) \frac{1}{\bar{l}N_v} \tag{8}$$

This size distribution is estimated from the TEM results.

3.2. Solid-solution strengthening

Atoms in solid solution give a considerable contribution σ_{ss} to the yield stress of the tested alloy. It is assumed that the strength contribution from each element can be added together [15,57]:

$$\sigma_{ss} = \sum_i k_i C_i^{\frac{2}{3}} \tag{9}$$

Here k_i are constants related with the size, modulus, and electronic mismatch of the specific element. The constants k_{Si}, k_{Mg}, k_{Cu} are given as 66.3 MPa/(wt%)$^{\frac{2}{3}}$, 29.0 MPa/(wt%)$^{\frac{2}{3}}$ and 46.4 MPa/(wt%)$^{\frac{2}{3}}$, respectively [15], and C_i is the mass fraction of each element in solid solution. From a theoretical point of view, this way of adding strength contributions from different solutes is strictly non-consistent. This is illustrated by that one gets another stress if one splits the concentration of one atom type into three and applies the formulae. However, the formulae is calibrated in earlier works and is pragmatically used here, providing reasonable estimates of the solute stress contributions.

3.2.1. Work hardening modelling

The work hardening is due to the stress contribution from the dislocations, σ_d, described by:

$$\sigma_d = M\tau = M\alpha\mu b\sqrt{\rho} \tag{10}$$

Here, M is the Taylor factor, ρ the dislocation density and α a constant in the range from 0.3 to 0.5. The generalized model by Kocks and Mecking [58] is applied for the evolution of the dislocation density ρ, i.e.

$$\frac{d\rho}{d\varepsilon_P} = M\frac{d\rho}{d\gamma} = M\left(\frac{2}{b\lambda} + \frac{2}{b\lambda_G} + \frac{2}{b\lambda_D} - k\rho \right) \tag{11}$$

Here b is the magnitude of the Burgers vector. The plastic strain is related, by $\varepsilon_P = \gamma/M$, to γ, the resolved shear strain (the standard effective one added from all slip systems). In plastically deformed materials, a distinction can be made between statistically stored dislocations (SSDs), which are stored by mutual random trapping, and GNDs. The first term on the right-hand side of Equation (11) models the athermal storage rate of SSDs. This term is inversely proportional to the mean free slip length, λ, of the SSDs. The second term models the athermal storage rate of GNDs and is inversely proportional to the geometrical slip length λ_G. This term contributes due to storage of dislocation loops generated by the non-shearable particles. The third term considers slip length restrictions from the grain boundaries, and $\lambda_D \approx D$, where D is the grain size. The last term handles the dynamic recovery of the dislocations, which in general cases depends on strain rate and temperature, but for a given temperature and a limited range of strain rates k is here kept constant for a given alloy condition.

The dislocations will form prismatic dislocation loops when interacting with the manganese containing dispersoids, formed during ho-

mogenization. Following Zhao and Holmedal [21], an estimate of the contribution to the athermal storage of GNDs is

$$\frac{d\rho_{\text{disp}}}{d\varepsilon_P} = M\frac{2}{b\lambda_{\text{disp}}}, \qquad \lambda_{\text{disp}} = \frac{2r_{\text{disp}}}{3\eta f_{\text{disp}}} \tag{12}$$

Here ρ_{disp} is the density of GNDs from the loops, f_{disp} is the volume fraction of dispersoids, r_{disp} is the average radius of the dispersoid particles and η is a constant of order unity. In theory [21], $\eta = 1$ for prismatic loops and $\eta = 1/2$ for shear loops or for prismatic loops when vacancy type loops are not formed. The latter value provided the best fit on the work by Zhao and Holmedal and is therefore also used here.

The potential formation of prismatic loops when a dislocation by-passes a non-shearable needle shaped precipitate, is not as simple as for the case of approximately spherical shaped dispersoids. Extensive cross-slip would have to be involved for the dislocation to overcome the length direction of the precipitate during the loop formation. Geometrically non-octahedral slip on {100}<011> slip systems would make it simpler, but since the {100} planes are not densely packed, the critical resolved shear stress will be large at room temperature. The authors are not aware of any experimental observation of prismatic loops punched out from needle shaped, non-shearable precipitates in AA6xxx alloys. According to Ashby [20], shear loops are unstable at strains beyond a few per cent, due to pile-ups, but the stress could be relaxed by some amount of cross glide along the needle shaped precipitate. The density of GNDs is here assumed to increase due to the shear loops formed around the needle-shaped precipitates, for which $d\rho_{\text{prec}}$ can be estimated for one particle as

$$d\rho_{\text{prec}} = n_o 2\left(1 + \sqrt{3}\right)\sqrt{a} \tag{13}$$

It is assumed that the dislocation length of one Orowan loop equals the cross-sectional perimeter of the precipitate needle in the slip plane it goes through, estimated as $2(1 + \sqrt{3})\sqrt{a}$. The number of dislocation loops per needle n_o can be estimated for the given shear strain, $d\gamma$, applied to the precipitate

$$\gamma = \frac{\sqrt{3}n_o b}{l} \tag{14}$$

Combining Equations (13) and (14) and integrating to sum up contributions to the athermal storage of dislocations from interactions with particles larger than their critical size for shearing, gives

$$\rho_{\text{prec}} = \int_{l_c}^\infty \frac{2(1 + \sqrt{3})l^2\,\gamma\,\varphi_l dl}{\sqrt{3}b\Omega}, \qquad \lambda_{\text{prec}}^{-1} = \frac{(1 + \sqrt{3})}{\sqrt{3}} \int_{l_c}^\infty \frac{l^2\,\varphi_l dl}{\Omega} \tag{15}$$

Note that for the special case of a narrow size distribution of non-shearable particles, $\rho_{\text{prec}} = 2(1 + \sqrt{3})f_v\gamma/\sqrt{3}\overline{a}b$, which may serve as a first approximation in overaged conditions. The total GND contribution from dispersoids and precipitates can be written:

$$\lambda_G^{-1} = \lambda_{\text{prec}}^{-1} + \lambda_{\text{disp}}^{-1} \tag{16}$$

The average slip length, λ_ρ due to SSDs, is commonly assumed to be controlled by dislocations. However, in the age hardened alloys the precipitates form a high density of strong obstacles that also will reduce the mean slip length of the dislocations. Hence a slip length, λ_p, based on the average distance between precipitate-based obstacles in the slip plane, should also be accounted for. Similar as argued for the strength contribution, the combination of these two slip lengths will be quadratic, and the total mean slip distance λ, of SSDs will be given by

$$\frac{1}{\lambda^2} = \frac{1}{\lambda_\rho^2} + \frac{1}{\lambda_p^2} \tag{17}$$

A well-established estimate for the dislocation-based slip length λ_ρ is applied, i.e., it is proportional to the average distance between dislocations:

$$\lambda_\rho = \frac{C}{\sqrt{\rho}} \tag{18}$$

Similar, λ_p is proportional to the average distance between non-shearable precipitate-based obstacles, written as:

$$\lambda_p = \frac{C_p}{\sqrt{n_p^{(ns)}}} \tag{19}$$

Here, $C_p \approx 30$ is applied. The area density $n_p^{(ns)}$ of obstacles from non-shearable precipitates can be estimated from the length distribution as

$$n_p^{(ns)} = \frac{\sqrt{3}}{3} \int_{l_c}^{\infty} l\varphi_l dl \tag{20}$$

Note that alternatively, Equation (18) can be expressed as $n_p^{(ns)} = f_v^{(ns)}/(\sqrt{3}\overline{a}^{(ns)})$, where $f_v^{(ns)}$ is the volume fraction and $\overline{a}^{(ns)}$ the mean cross-sectional area of the non-shearable precipitates. Hence the basic length scale is $\sqrt{f_v^{(ns)}/\overline{a}^{(ns)}}$, as compared to $f_v^{(ns)}/\sqrt{\overline{a}^{(ns)}}$ for the GND storage mechanism.

4. Modelling-results and discussion

4.1. Strength modelling

The stress component σ_0 is put equal to 35 MPa, corresponding approximately to the initial stress in a tensile test of commercial pure aluminum, but also accounting for strength contributions from dispersoids and the grain size, which are small compared to the main contribution from the precipitates. The stress from the solutes σ_{ss} can be estimated by Equation (9) using the solute concentrations listed in Table 4. The calculated σ_{ss} evolution is presented in Fig. 5(a). As a consequence of precipitate nucleation, growth and coarsening, it declines with increased aging time. As the stress contribution of the solute is approximately 80 MPa for the as quenched condition, the estimated yield strength is 115 MPa, which is within the error of the experimental measured initial yield stress.

Fig. 5(a) also presents the change of the stress component σ_p with aging time. It increases from 177 MPa after 20 min to 303 MPa after 12 h aging. It drops only slightly to 293 MPa after 24 h aging but softens considerable after 1 week and beyond.

Fig. 5(b) shows a comparison of the estimated strengths by the proposed model and experimental data at each aging condition. The factor $\alpha_p = 0.66$ provides a good overall fit. A good agreement with experiments verifies the accuracy of the proposed strength model. The maximum deviation is about 32% for the condition with one-week aging, while the minimum deviation is about 1%, corresponding to 12 h aging. The deviation for the peak aged condition is small, within 2%. The estimates tend to be too low at the under aged conditions and too high at overaged conditions. At overaged conditions, the precipitate strength contributions vary for different precipitate phases present. Furthermore, fewer and larger particles make the TEM statistics less reliable.

4.1.1. Work hardening at large strains

In their work, Cheng et al. [30] made the simplifying assumption that the stress contribution from the dislocations, σ_d, was the same for all aged conditions. Their $\sigma_d(\varepsilon)$ curves were based on the tensile test of the ssss condition, from which $\sigma_d(\varepsilon)$ was directly measured. However, $\sigma_d(\varepsilon)$ will be different after different aging times, as the elements in solid solution are consumed by the precipitates. However, even at the severely overaged conditions, some level of solute remains in the matrix.

In this work, the solute concentrations are estimated based on a detailed characterization of the precipitates. It is expected that σ_d varies approximately linearly with the concentration of elements in solid so-
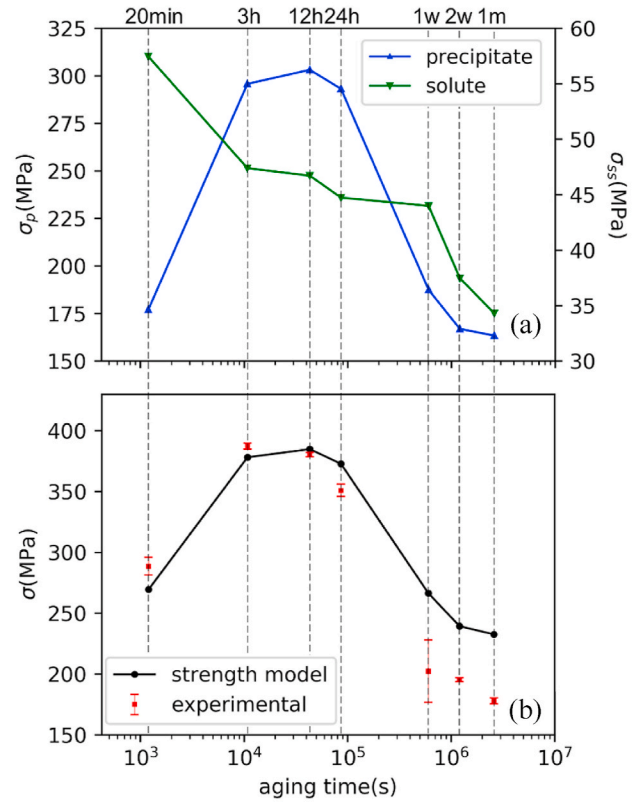

Fig. 5. (a) Stress contribution from precipitates and atoms in solid solution as a function of the aging time. (b) Comparison of experimental yield strength and predicted yield strength for the AA6082 alloy aged at 180 °C to various aging times.

lution [59]. Hence, an estimate of how $\sigma_d(\varepsilon)$ varies with the level of solute concentration is made by assuming that σ_d, at a given strain ε, increases linearly with the solute concentration, $C_{Mg} + C_{Si} + C_{Cu}$, i.e., between the curves of the commercially pure aluminum alloy and the ssss. In both these cases, without the precipitates, $\sigma_d(\varepsilon)$ can be derived directly from the respective stress-strain curve. Hence a necking corrected stress-strain curve was obtained from a tensile test of a DC-cast commercially 99% pure (2 N) alloy with a grain size of about 100 μm. Note that the Taylor factor, $M = 2.82$, is applied for the random texture, calculated by the ALAMEL model [60]. This is a smaller value than the commonly applied estimate by the simpler full-constraint Taylor model but more in accordance with crystal plasticity finite element calculations [61]. Corrections were made to find a 2 N curve for the same Taylor factor as the ssss curve, i.e., $\sigma_d \rightarrow \sigma_d M_{ssss}/M_{pure}$ and $\varepsilon \rightarrow \varepsilon M_{pure}/M_{ssss}$.

The tensile tests curves by Cheng et al. [30] were limited by the uniform strain. It is interesting to firstly extend their analysis and see how it applies at the larger strains measured as part of this work. At the underaged and peak aged conditions the geometrical slip length restrictions are small, and Cheng et al. [30] assumed they could be ignored. Hence, when knowing σ_d and σ_p and the coefficient n, the stress-strain curves could be obtained by Equation (4). To provide estimates of σ_d up to larger strains, calibrations of the 2 N and ssss curves were made up to a strain of 50%, and $\sigma_d(\varepsilon)$ curves for the aged conditions were obtained by interpolation as explained above. The smaller grain size and the dispersoids in the AA6082 will introduce some extra initial work hardening that here in the large strain estimates will be ignored. These contributions will, however, be considered below, in the more detailed analysis at smaller strains.

Following the work by Cheng et al. [30], the values of n that provide the best fit up to the uniform strain, were chosen, and the results are

shown in Fig. 6(a) and (c) for the 20 min and the 3 h curves. For the case of 20 min aging, a simple addition of the terms (i.e., $n = 1$) gives a very good fit, while at 3 h aging, $n = 1.3$ gives the best fit. Note, however that at larger strains, the measured aged curves show much less work hardening. It is obvious that the stress-strain behavior at large strain is different with the presence of the precipitates than without. In the peak aged 3 h condition the curve is completely flat, indicating that a different dynamic recovery mechanism is invoked due to the precipitates.

From a physical point of view, each obstacle provided by the precipitates is rather weak after 20 min aging, justifying adding the stress terms for this case. This provided a good fit of the stress-strain curve in Fig. 6(a). Hence the linear interpolation of σ_d between ssss and the 2 N alloy is regarded a good approximation. However, after 3 h aging the precipitates act as strong obstacles, of similar strength as the dislocation-based obstacles, and $n = 2$ should be expected, according to the theory.

Another important result from Fig. 6(b) and (d), is that at larger strains, the stress-strain curves become significantly flatter than predicted by any choice of n. The 3 h curve shows no work hardening beyond a strain of about 15%. This means that the dynamic recovery is strongly influenced by the presence of the precipitates. The modelling of the influence of precipitates on the dynamic recovery is very interesting but beyond the scope of this work.

4.2. Work-hardening modelling

According to the proposed model, which follows the work by Cheng et al. [30], the work hardening is given by:

$$\frac{d\sigma_f}{d\varepsilon} = \left(\frac{\sigma_p}{\left(\sigma_p^n + \sigma_d^n\right)^{\frac{1}{n}}}\right)^{n-1} \frac{d\sigma_p}{d\varepsilon} + \left(\frac{\sigma_d}{\left(\sigma_p^n + \sigma_d^n\right)^{\frac{1}{n}}}\right)^{n-1} \frac{d\sigma_d}{d\varepsilon} \qquad (21)$$

To assess the qualitative results from the modelling work by Cheng et al. [30], an increased level of precision will be aimed in the current work. The precipitates were accounted for based on detailed TEM statistics, both when determining the geometrical slip length restrictions, when calculating σ_p, and when estimating the solute dependency of σ_d. Furthermore, a new mechanism is proposed for slip length restriction imposed by the precipitates, by that the total mean slip distance of SSDs is modified. Hence, if λ_p is ignored, the model will be consistent with the model by Cheng et al. [30]. The results obtained by this approximation will be referred to as "model 1".

The basic idea behind the geometrical slip length is the formation of GNDs in form of Orowan loops around the precipitates or prismatic loops. It is questionable if prismatic loops can form from needle-shaped precipitates, the authors are not aware of any observation of that. The loops contribute to the dislocation density and are assumed to increase the number of dislocation-based obstacles for the mobile dislocations. However, Orowan loops formed around a needle shaped particle will form obstacles at the same location as the particle itself forms a strong obstacle. A relevant question is if this obstacle can be counted twice? Hence in a second variant, denoted "model 2", λ_{prec} is ignored (i.e., $\lambda_G = \lambda_{disp}$), while λ_p is included. An exception is the 20 min condition, for which the precipitates are weak obstacles that do not influence the work hardening, i.e., model 1 and model 2 are equal in this case. A third case could be to include the influence of the precipitates both in terms of λ_G and λ_p, which would give the strongest work hardening. However, the work hardening in this third case turns out to be unrealistic high, hence it is not included in the presented results.

Note that a simple one-parameter work-hardening model like the one considered here, is not valid at large strains. Furthermore, it is clear from Fig. 6 that the dynamic recovery is significantly different at larger strains, hence only strains up to 15% will be considered for calibrating the models. At peak and over aged conditions, the particles act as strong dislocation obstacles, and it is reasonable to assume $n = 2$, while for the 20 min aging the particles are weak and $n = 1$, resulting in equal results for both model 1 and model 2 in Fig. 8(a) for this case.

In the work hardening model, $\sigma_d = M\alpha\mu\sqrt{\rho}$ is given by the solution of Equation (11). For ssss and 2 N, i.e., the alloys without precipitates, the constants k and C can be calibrated from the measured curves. Note that
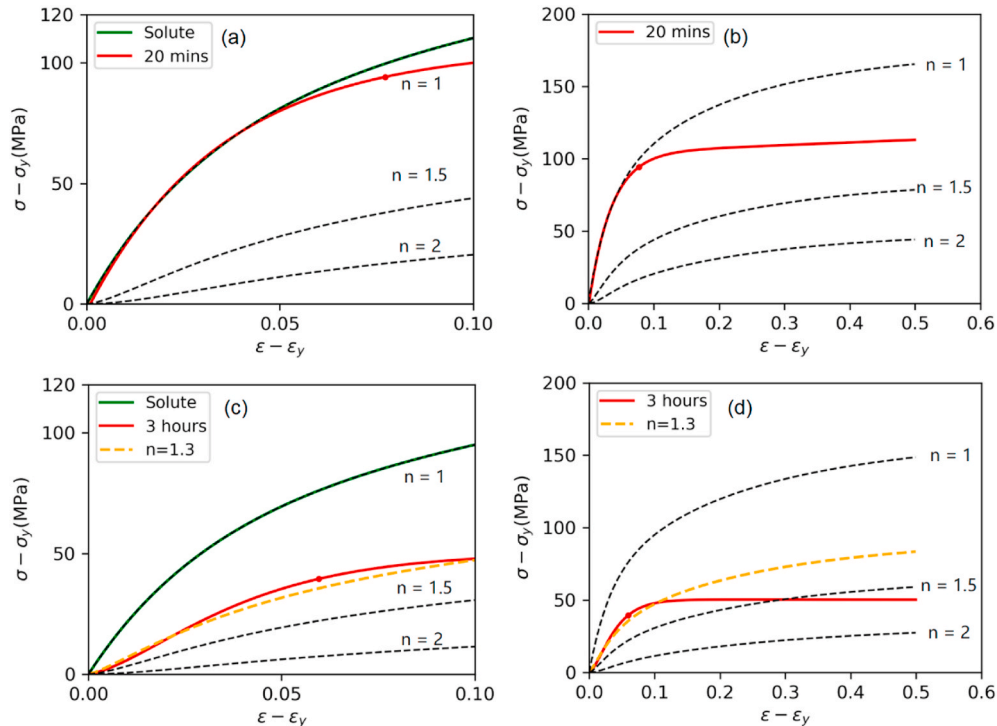

Fig. 6. Stress-strain curves by the model by Cheng et al. [30] compared to the experimental curves for material aged at 20 min (a, b) and the peak aged condition in (c, d). The detailed stress-strain curves at strains up to 0.1 are shown in (a, c).

the different grain sizes for these two conditions are now accounted for, as this contribution cannot be ignored at small strains. In order to estimate the $\sigma_d(\varepsilon)$ curves for the aged conditions, σ_d at each strain ε, is linear interpolated as a function of the solute concentration, being estimated by $C_{Mg} + C_{Si} + C_{Cu}$. Interpolation is performed between ssss and 2 N stress-strain curves, as calculated by the calibrated model, while setting the grain size infinitely large and the Taylor factor $M = 3.05$ in the model. For each of the interpolated stress-strain curves, k and C are given in Table 5. The interpolated $\sigma_d(\varepsilon)$ curves are shown in Fig. 7, These curves are then used for calibrating k and C for each ageing condition, being required for running model 1 and model 2. In the work hardening models, the following parameters are applied: $\alpha = 0.3, \mu = 27GPa, b = 0.287nm$.

Fig. 8(b–g) shows model results for peak and over-aged conditions. In general model 2, with the new model for the slip-length restriction due to precipitates, gives a good agreement with the experiments, while model 1 predicts too strong work hardening, i.e., with slip-length restriction based on storage of GNDs around precipitates.

In Fig. 8(b), for the peak aged condition, the black dashed line represents model 2, but without the contribution from λ_p, i.e., making the slip length not being influenced by the precipitates. The low initial work hardening is then solely due to the nonlinear mixing of a strong work hardening contribution from σ_d and no work hardening from σ_p, as described by Equation (21) with $n = 2$. This is the result, if assuming, similar as Cheng et al. [30], that the precipitates do not contribute to storage of GNDs in the peak aged condition, i.e. that most of the precipitates are shearable. The mechanism proposed by model 2 provides the right amount of work hardening. If model 1 should predict a lower, reasonable work hardening in this case, λ_G would have to be larger, which would be the case if fewer particles were non-shearable, i.e., the critical precipitate size for the non-shearable transition was reached considerably later than at the peak aged condition. Recent high-resolution TEM might indicate that this may be the case [62], hence this alternative explanation cannot be completely ruled out.

The precise counting of precipitates in TEM is not an easy task. Even though a thorough counting is performed in Ref. [18], precipitate size statistics that are representative for the bulk sample is always challenging to obtain. Even though it can be discussed how representative the quantitative detailed measurements are for the alloys, the results are qualitatively good, and the same procedures are applied for all aged conditions. Hence, the large difference between the two models justifies the conclusion, that the suggested model 2 for the influence of the precipitates on the slip length restrictions on the SSDs provides a more realistic work hardening than accounting for geometrical necessary dislocations by model 1. As discussed by Holmedal [63], the slip length is restricted by dislocation obstacles. It is reasonable to also count the precipitate-based obstacles, at least the strongest ones. In the suggested model 1, only precipitates larger than the critical size are included when calculating this contribution. However, this limit is not necessarily correlated with the shearable versus non-shearable transition, but rather with when the obstacles for dislocation glide contributed by the precipitates get similar cutting strength as the dislocation-based obstacles.

5. Conclusion

The yield stress and work hardening of age hardened Al–Mg–Si alloy have been analyzed and modelled based on input from detailed TEM characterization of the precipitate structure and compared to necking corrected tensile tests at different aging conditions. It is concluded that the work hardening at strains beyond necking is severely suppressed due to the presence of precipitates, with no work hardening at all for the peak aged condition. At strains up to about 15%, the yield stress and work hardening are modelled by accounting for the detailed precipitate size distribution, when estimating the particle stress contribution and the slip length restrictions. A refined version of the classical estimate of

Table 5
k and C from interpolated curves, for each ageing condition.

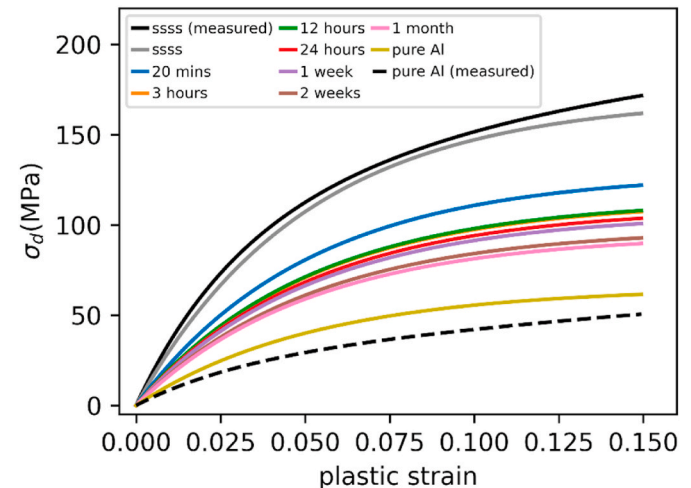| Aging time	20 min	3 h	12 h	24 h	1 week	2 weeks	1 month
C	22.04	25.15	25.00	26.07	26.86	29.24	30.30
k	15.05	14.98	14.98	14.95	15.14	14.89	14.86

Fig. 7. Estimated σ_d without GNDs and for an infinite grain size as a function of plastic strain, for different solute levels at each aging condition, required for the calibration of C and k in Table 5. First, calibrations of the model are made to the 2 N aluminum curve and ssss curve, accounting for dispersoids, grain size and the Taylor factor. These two curves are included in the figure. Then the plotted curves are found by linear interpolation as a function of the solute concentration between these two curves, using M = 3.05 (for the AA6082 texture) in the model.

the storage rate of GNDs by dislocation looping of non-shearable precipitates is developed. However, this mechanism overestimates the work hardening, and it is concluded that it is either not acting, or the shearable transition occurs for particles that are considerable larger than the average size at the peak aged condition. Instead, a new mechanism for the slip length restriction, based on treating precipitate based and dislocation-based obstacles in a similar way, is suggested. This model provides realistic results for peak- and overaged conditions.

Data availability

The raw data required to reproduce these findings cannot be shared at this time due to technical or time limitations. The processed data required to reproduce these findings are available from https://gitlab.com/ntnu-physmet/necking-correction/-/tree/master/MSEA paper2022 and https://ars.els-cdn.com/content/image/1-s2.0-S0921509321001313-mmc1.pdf.

Credit author statement

Feng Lu: Investigation, Conceptualization, Methodology, Software, Writing – original draft preparation, Writing- Reviewing and Editing. **Jonas. K. Sunde**: Methodology. **Calin. D. Marioara**: Supervision. **Randi Holmestad**: Supervision. **Bjørn Holmedal**: Conceptualization, Methodology, Supervision, Writing- Reviewing and Editing.

Declaration of competing interest

The authors declare that they have no known competing financial interests or personal relationships that could have appeared to influence
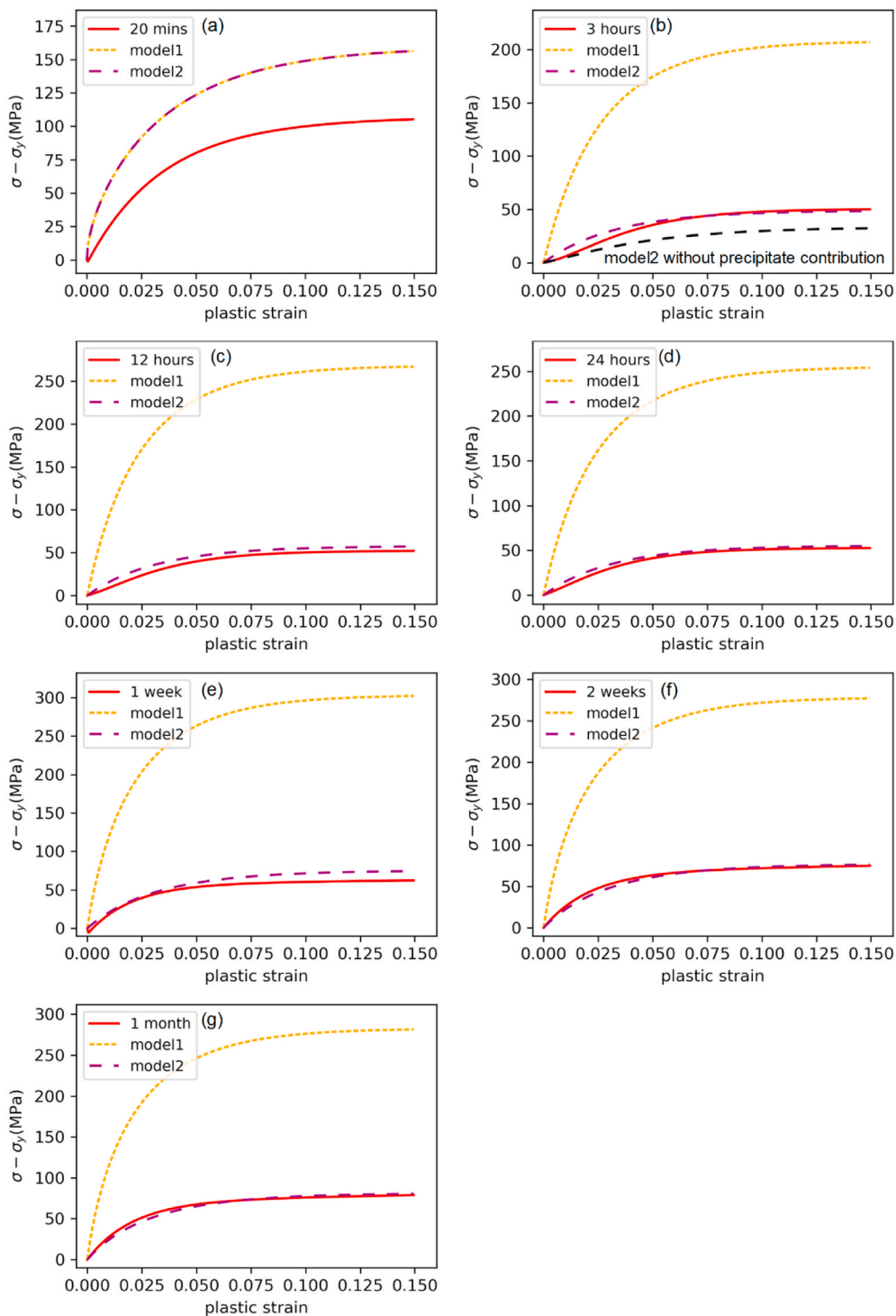
Fig. 8. Comparison of stress-strain curves up to 15% strain for the two models and the tensile tests; aged at 20 min (a), 3 h (b), 12 h (c), 24 h (d), 1 week (e), 2 weeks (f) and 1 month (g).

the work reported in this paper.

References

[1] M. Tisza, I. Czinege, Comparative study of the application of steels and aluminium in lightweight production of automotive parts, Int. J. Light. Mater. Manuf. 1 (2018) 229–238, https://doi.org/10.1016/j.ijlmm.2018.09.001.

[2] M. Yang, H. Chen, A. Orekhov, Q. Lu, X. Lan, K. Li, S. Zhang, M. Song, Y. Kong, D. Schryvers, Y. Du, Quantified contribution of β″ and β′ precipitates to the

strengthening of an aged Al–Mg–Si alloy, Mater. Sci. Eng. A. 774 (2020) 138776, https://doi.org/10.1016/j.msea.2019.138776.

[3] C.D. Marioara, S.J. Andersen, H.W. Zandbergen, R. Holmestad, The influence of alloy composition on precipitates of the Al-Mg-Si system, Metall. Mater. Trans. A. 36 (2005) 691–702, https://doi.org/10.1007/s11661-005-0185-1.

[4] I. Dutta, S.M. Allen, A calorimetric study of precipitation in commercial aluminium alloy 6061, J. Mater. Sci. Lett. 10 (1991) 323–326, https://doi.org/10.1007/BF00719697.

[5] Q. Du, B. Holmedal, J. Friis, C.D. Marioara, Precipitation of non-spherical particles in aluminum alloys Part II: numerical simulation and experimental characterization during aging treatment of an Al-Mg-Si alloy, Metall. Mater. Trans. A. 47 (2016) 589–599, https://doi.org/10.1007/s11661-015-3196-6.

[6] B. Holmedal, Strength contributions from precipitates, Philos. Mag. Lett. 95 (2015) 594–601, https://doi.org/10.1080/09500839.2015.1125029.

[7] Y. Li, B. Holmedal, H. Li, L. Zhuang, J. Zhang, Q. Du, Precipitation and strengthening modeling for disk-shaped particles in aluminum alloys: size distribution considered, Materialia 4 (2018) 431–443, https://doi.org/10.1016/j.mtla.2018.11.001.

[8] T. Khelfa, M.A. Rekik, J.A. Muñoz-Bolaños, J.M. Cabrera-Marrero, M. Khitouni, Microstructure and strengthening mechanisms in an Al-Mg-Si alloy processed by equal channel angular pressing (ECAP), Int. J. Adv. Manuf. Technol. 95 (2018) 1165–1177, https://doi.org/10.1007/s00170-017-1310-1.

[9] D. Bardel, M. Perez, D. Nelias, A. Deschamps, C.R. Hutchinson, D. Maisonnette, T. Chaise, J. Garnier, F. Bourlier, Coupled precipitation and yield strength modelling for non-isothermal treatments of a 6061 aluminium alloy, Acta Mater 62 (2014) 129–140, https://doi.org/10.1016/j.actamat.2013.09.041.

[10] O.R. Myhr, O. Børvik, C.D. Marioara, S. Wenner, O.S. Hopperstad, Nanoscale modelling of combined isotropic and kinematic hardening of 6000 series aluminium alloys, Mech. Mater. (2020) 105398, https://doi.org/10.1016/j.mechmat.2020.103603.

[11] H.S. Hasting, A.G. Frøseth, S.J. Andersen, R. Vissers, J.C. Walmsley, C.D. Marioara, F. Danoix, W. Lefebvre, R. Holmestad, Composition of β″ precipitates in Al–Mg–Si alloys by atom probe tomography and first principles calculations, J. Appl. Phys. 106 (2009) 123527, https://doi.org/10.1063/1.3269714.

[12] W.J. Poole, X. Wang, D.J. Lloyd, J.D. Embury, The shearable-non-shearable transition in Al-Mg-Si-Cu precipitation hardening alloys: implications on the distribution of slip, work hardening and fracture, Philos. Mag. 85 (2005) 3113–3135, https://doi.org/10.1080/14786430500154935.

[13] M. Vivas, P. Lours, C. Levaillant, A. Couret, M.-J. Casanove, A. Coujou, Determination of precipitate strength in aluminium alloy 6056-T6 from transmission electron microscopy in situ straining data, Philos. Mag. A. 76 (1997) 921–931, https://doi.org/10.1080/01418619708200007.

[14] A. Deschamps, Y. Brechet, Influence of predeformation and aging of an Al-Zn-Mg alloy-II. Modeling of precipitation kinetics and yield stress, Acta Mater 47 (1998) 293–305, https://doi.org/10.1016/S1359-6454(98)00296-1.

[15] O.R. Myhr, O. Grong, S.J. Andersen, Modelling of the age hardening behaviour of Al-Mg-Si alloys, Acta Mater 49 (2001) 65–75, https://doi.org/10.1016/S1359-6454(00)00301-3.

[16] O.R. Myhr, O.S. Hopperstad, T. Børvik, A combined precipitation, yield stress, and work hardening model for Al-Mg-Si alloys incorporating the effects of strain rate and temperature, Metall. Mater. Trans. A. 49 (2018) 3592–3609, https://doi.org/10.1007/s11661-018-4675-3.

[17] S. Esmaeili, D.J. Lloyd, W.J. Poole, A yield strength model for the Al-Mg-Si-Cu alloy AA6111, Acta Mater 51 (2003) 2243–2257, https://doi.org/10.1016/S1359-6454(03)00028-4.

[18] J.K. Sunde, F. Lu, C.D. Marioara, B. Holmedal, R. Holmestad, Linking mechanical properties to precipitate microstructure in three Al-Mg-Si(-Cu) alloys, Mater. Sci. Eng. A. 807 (2021) 140862, https://doi.org/10.1016/j.msea.2021.140862.

[19] Q. Du, K. Tang, C.D. Marioara, S.J. Andersen, B. Holmedal, R. Holmestad, Modeling over-ageing in Al-Mg-Si alloys by a multi-phase CALPHAD-coupled Kampmann-Wagner Numerical model, Acta Mater 122 (2017) 178–186, https://doi.org/10.1016/j.actamat.2016.09.052.

[20] M.F. Ashby, The deformation of plastically non-homogeneous materials, Philos. Mag. 21 (1970) 399–424, https://doi.org/10.1080/14786437008238426.

[21] Q. Zhao, B. Holmedal, Modelling work hardening of aluminium alloys containing dispersoids, Philos. Mag. 93 (2013) 3142–3153, https://doi.org/10.1080/14786435.2013.805271.

[22] J. Friis, B. Holmedal, Ø. Ryen, E. Nes, O.R. Myhr, Ø. Grong, T. Furu, K. Marthinsen, Work hardening behaviour of heat-treatable Al-Mg-Si-alloys, Mater. Sci. Forum. (2006) 519–521. https://doi.org/10.4028/www.scientific.net/msf.519-521.1901, 1901–1906.

[23] M. Ghosh, A. Miroux, L.A.I. Kestens, Experimental study and modelling of the role of solutes, precipitates and temperature on the work-hardening of AA6xxx aluminium alloys, Mater. Sci. Eng. A. 805 (2021) 140615, https://doi.org/10.1016/j.msea.2020.140615.

[24] E. Nes, Modelling of work hardening and stress saturation in FCC metals, Prog. Mater. Sci. 41 (1997) 129–193, https://doi.org/10.1016/S0079-6425(97)00032-7.

[25] B. Holmedal, K. Marthinsen, E. Nes, A unified microstructural metal plasticity model applied in testing, processing, and forming of aluminium alloys, Zeitschrift Für Met. 96 (2005) 532–545, https://doi.org/10.3139/146.101067.

[26] O.R. Myhr, Ø. Grong, C. Schäfer, An extended age-hardening model for Al-Mg-Si alloys incorporating the room-temperature storage and cold deformation process stages, Metall. Mater. Trans. A. 46 (2015) 6018–6039, https://doi.org/10.1007/s11661-015-3175-y.

[27] O.R. Myhr, O. Grong, S. Klokkehaug, H.G. Fjoer, A.O. Kluken, Process model for welding of Al-Mg-Si extrusions Part 1: precipitate stability, Sci. Technol. Weld. Join. 2 (1997) 245–253, https://doi.org/10.1179/136217197791069911.

[28] U.F. Kocks, H. Mecking, Physics and phenomenology of strain hardening: the FCC case, Prog. Mater. Sci. 48 (2003) 171–273, https://doi.org/10.1016/S0079-6425(02)00003-8.

[29] U.F. Kocks, A.S. Argon, M.F. Ashby, Thermodynamics and kinetics of slip, Prog. Mater. Sci. 19 (1975) 1–291.

[30] L.M. Cheng, W.J. Poole, J.D. Embury, D.J. Lloyd, The influence of precipitation on the work-hardening behavior of the aluminum alloys AA6111 and AA7030, Metall. Mater. Trans. A. 34 (2003) 2473–2481, https://doi.org/10.1007/s11661-003-0007-2.

[31] C. Defaisse, M. Mazière, L. Marcin, J. Besson, Ductile fracture of an ultra-high strength steel under low to moderate stress triaxiality, Eng. Fract. Mech. 194 (2018) 301–318, https://doi.org/10.1016/j.engfracmech.2017.12.035.

[32] G.H. Majzoobi, F. Fariba, M.K. Pipelzadeh, S.J. Hardy, A new approach for the correction of stress-strain curves after necking in metals, J. Strain Anal. Eng. Des. 50 (2015) 125–137, https://doi.org/10.1177/0309324714555384.

[33] J.H. Kim, A. Serpantié, F. Barlat, F. Pierron, M.G. Lee, Characterization of the post-necking strain hardening behavior using the virtual fields method, Int. J. Solids Struct. 50 (2013) 3829–3842, https://doi.org/10.1016/j.ijsolstr.2013.07.018.

[34] L. Wang, W. Tong, Identification of post-necking strain hardening behavior of thin sheet metals from image-based surface strain data in uniaxial tension tests, Int. J. Solids Struct. (2015) 12–31, https://doi.org/10.1016/j.ijsolstr.2015.04.038, 75–76.

[35] M. Usami, T. Oya, Estimation of work-hardening curve for large strain using friction-free compression test, Procedia Eng 81 (2014) 371–376, https://doi.org/10.1016/j.proeng.2014.10.008.

[36] V. Vilamosa, A.H. Clausen, E. Fagerholt, O.S. Hopperstad, T. Børvik, Local measurement of stress-strain behaviour of ductile materials at elevated temperatures in a split-hopkinson tension bar system, Strain 50 (2014) 223–235, https://doi.org/10.1111/str.12084.

[37] P. Siegmann, C. Alén-Cordero, R. Sánchez-Montero, Experimental approach for the determination of the Bridgman's necking parameters, Meas. Sci. Technol. 30 (2019) 114003, https://doi.org/10.1088/1361-6501/ab2a4f.

[38] F. Lu, T. Mánik, I.L. Andersen, B. Holmedal, A robust image processing algorithm for optical based stress-strain curve corrections after necking, J. Mater. Eng. Perform. (2021) in press.

[39] O.R. Myhr, Ø. Grong, Modelling of non-isothermal transformations in alloys containing a particle distribution, Acta Mater 48 (2000) 1605–1615, https://doi.org/10.1016/S1359-6454(99)00435-8.

[40] A. Deschamps, F. Livet, Y. Bréchet, Influence of predeformation on ageing in an Al-Zn-Mg alloy-I. Microstructure evolution and mechanical properties, Acta Mater 47 (1998) 281–292, https://doi.org/10.1016/S1359-6454(98)00293-6.

[41] D.W. Scott, Kernel Density Estimators, Wiley, New York, 1992, pp. 125–193, https://doi.org/10.1002/9780470316849.ch6.

[42] J.K. Sunde, C.D. Marioara, A.T.J. van Helvoort, R. Holmestad, The evolution of precipitate crystal structures in an Al-Mg-Si(-Cu) alloy studied by a combined HAADF-STEM and SPED approach, Mater. Charact. 142 (2018) 458–469, https://doi.org/10.1016/j.matchar.2018.05.031.

[43] A.L. Dons, E.K. Jensen, Y. Langsrud, E. Trømborg, S. Brusethaug, The alstruc microstructure solidification model for industrial aluminum alloys, Metall. Mater. Trans. A. 30 (1999) 2135–2146, https://doi.org/10.1007/s11661-999-0025-9.

[44] A. Lise Dons, The Alstruc homogenization model for industrial aluminum alloys, J. Light Met. 1 (2001) 133–149, https://doi.org/10.1016/S1471-5317(01)00007-4.

[45] F. Lu, H.M. Asadkandi, T. Mánik, I.L. Andersen, B. Holmedal, Necking Correction, 2020. https://gitlab.com/ntnu-physmet/necking-correction.

[46] F. Lu, T. Mánik, B. Holmedal, Stress corrections after necking using a two-parameter equation for the radius of curvature, J. Appl. Mech. 88 (2021), 061006, https://doi.org/10.1115/1.4050474.

[47] M. Gromada, G. Mishuris, A. Öchsner, Correction Formulae for the Stress Distribution in Round Tensile Specimens at Neck Presence, Springer, Berlin Heidelberg, 2011, https://doi.org/10.1007/978-3-642-22134-7.

[48] A.D. Rollett, U.F. Kocks, A review of the stages of work hardening, in: Dislocations '93, Trans Tech Publications Ltd, 1993, pp. 1–18. https://doi.org/10.4028/www.scientific.net/SSP.35-36.1.

[49] Ø. Ryen, H.I. Laukli, B. Holmedal, E. Nes, Large strain work hardening of aluminium alloys and the effect of mg in solid solution, Metall. Mater. Trans. A. 37 (2006) 2007–2013, https://doi.org/10.1007/s11661-006-0143-6.

[50] O.R. Myhr, Ø. Grong, K.O. Pedersen, A combined precipitation, yield strength, and work hardening model for Al-Mg-Si alloys, Metall. Mater. Trans. A. 41 (2010) 2276–2289, https://doi.org/10.1007/s11661-010-0258-7.

[51] N. Hansen, The effect of grain size and strain on the tensile flow stress of aluminium at room temperature, Acta Metall 25 (1977) 863–869, https://doi.org/10.1016/0001-6160(77)90171-7.

[52] Q. Zhao, M. Slagsvold, B. Holmedal, Comparison of the influence of Si and Fe in 99.999% purity aluminum and in commercial-purity aluminum, Scr. Mater. 67 (2012) 217–220, https://doi.org/10.1016/j.scriptamat.2012.04.023.

[53] A. de Vaucorbeil, C.W. Sinclair, W.J. Poole, Dislocation glide through non-randomly distributed point obstacles, Philos. Mag. 93 (2013) 3664–3679, https://doi.org/10.1080/14786435.2013.820384.

[54] A. de Vaucorbeil, W.J. Poole, C.W. Sinclair, The effect of obstacle strength distribution on the critical resolved shear stress of engineering alloys, Mater. Sci. Forum. (2014) 794–796. https://doi.org/10.4028/www.scientific.net/MSF.794-796.449, 449–454.

[55] P. Van Houtte, S. Li, M. Seefeldt, L. Delannay, Deformation texture prediction: from the Taylor model to the advanced Lamel model, Int. J. Plast. 21 (2005) 589–624, https://doi.org/10.1016/j.ijplas.2004.04.011.

[56] A.J. Ardell, Precipitation hardening, Metall. Trans. A. 16 (1985) 2131–2165, https://doi.org/10.1007/BF02670416.

[57] H.R. Shercliff, M.F. Ashby, A process model for age hardening of aluminium alloys-I. The model, Acta Metall. Mater. 38 (1990) 1789–1802, https://doi.org/10.1016/0956-7151(90)90291-N.

[58] H. Mecking, U.F. Kocks, Kinetics of flow and strain-hardening, Acta Metall 29 (1981) 1865–1875, https://doi.org/10.1016/0001-6160(81)90112-7.

[59] Ø. Ryen, B. Holmedal, O. Nijs, E. Nes, E. Sjölander, H.-E. Ekström, Strengthening mechanisms in solid solution aluminum alloys, Metall. Mater. Trans. A. 37 (2006) 1999–2006, https://doi.org/10.1007/s11661-006-0142-7.

[60] K. Zhang, B. Holmedal, O.S. Hopperstad, S. Dumoulin, J. Gawad, A. Van Bael, P. Van Houtte, Multi-level modelling of mechanical anisotropy of commercial pure aluminium plate: crystal plasticity models, advanced yield functions and parameter identification, Int. J. Plast. 66 (2015) 3–30, https://doi.org/10.1016/j.ijplas.2014.02.003.

[61] K. Zhang, B. Holmedal, T. Mánik, A. Saai, Assessment of advanced Taylor models, the Taylor factor and yield-surface exponent for FCC metals, Int. J. Plast. 114 (2019) 144–160, https://doi.org/10.1016/j.ijplas.2018.10.015.

[62] E. Christiansen, C.D. Marioara, B. Holmedal, O.S. Hopperstad, R. Holmestad, Nano-scale characterisation of sheared β″ precipitates in a deformed Al-Mg-Si alloy, Sci. Rep. 9 (2019) 1–11, https://doi.org/10.1038/s41598-019-53772-4.

[63] B. Holmedal, On the basic relation between mean free slip length and work hardening of metals, Philos. Mag. 95 (2015) 2817–2830, https://doi.org/10.1080/14786435.2015.1082038.